

Thunderstorm Cloud Top Dynamics as Inferred from Satellite Observations and a Cloud Top Parcel Model

ROBERT F. ADLER

Laboratory for Atmospheres, NASA/Goddard Space Flight Center, Greenbelt, MD 20771

ROBERT A. MACK

General Software Corporation, Landover, MD 20785

(Manuscript received 22 August 1985, in final form 17 March 1986)

ABSTRACT

A Lagrangian model applicable to the overshooting region of thunderstorm tops is used to describe the temperature–height path taken by updraft core parcels as they penetrate above the tropopause, reach their maximum height, and descend in the periphery of the convective tower. The model is run under a variety of ambient and in-cloud conditions in order to simulate certain temperature–height relationships observed in satellite observations.

Observations indicate that in the majority of observed storm tops, the satellite-observed cold point in the IR brightness temperature (T_B) field is collocated with the highest point in the convective overshooting region and the T_B –height relations are near adiabatic. The parcel model quantitatively reproduces this type of relationship for model runs where the mixing parameter is relatively small.

Another type of storm has a close-in, cold–warm T_B couplet with a dimension of approximately 20–40 km and a V-shaped cold T_B pattern. In some cases of these V-shaped storms, the cold point is clearly located upwind of the high point. Model runs have been made to reproduce a number of these salient features for these types of storms. With larger values of the mixing parameters (presumably related to larger shear), the model produces temperature–height relationships that are, of course, much closer to ambient than to adiabatic, as is observed in these cases. With the larger mixing parameter, the cold–high offset is also produced, for model runs having a relatively large initial vertical velocity and under conditions of a strong inversion. The amount of the cold–high offset is shown to be a direct function of the strength of the inversion.

The cause of the close-in warm point is also explored with the simple model. As has been shown in three-dimensional cloud model results, the warm point in the cold–warm couplet can be related to internal cloud subsidence on the downwind side in association with mixing with the environment. This effect is also reproduced in the parcel model with the occurrence of a warm point being related to conditions of an intense updraft and strong mixing. The model also points to parcels subsiding from their maximum height and crossing the ambient lapse rate from negative to positive buoyancy on the downwind side and then coming into equilibrium at a relatively high level above the tropopause on the downwind side. This effect may be related to the top of the downwind anvil cloud being elevated significantly above the equilibrium point or tropopause. Another interpretation of this model result may be related to the above-anvil cirrus noted by a few investigators.

The temperature–height distributions produced by the model in a Lagrangian framework are converted to the spatial domain by the assumption of steady state conditions and are compared to temperature–height cross sections determined from GOES IR and stereoscopic height fields. The locations of cold points, high points, warm points, and the magnitude of cold–high offsets compare favorably between the model and the satellite observations.

1. Introduction

Satellite observations of convective towers penetrating the tropopause have revealed a number of characteristics that need to be explained in order to enhance our understanding of cloud top processes and also in order to infer cloud top height from satellite infrared (IR) data and storm intensity from the same observations. In this paper, GOES¹ IR data, GOES stereoscopic observations, AVHRR² (1 km IR resolution) data, and

aircraft overflight data are summarized to examine thunderstorm top temperature–height structure and temperature–height conversion relations in the convective, overshooting top region. Three classes of storm tops are described and the causes of their unique temperature–height structures are explored with a one-dimensional cloud parcel model applied in the overshooting region.

2. Satellite-observed thunderstorm top structure

Thunderstorm tops typically appear in 11 micron infrared (IR) satellite images as points of relative min-

¹ Geostationary Operational Environmental Satellite.

² Advanced Very High Resolution Radiometer.

imum in IR brightness temperature, T_B (Adler and Fenn, 1979; Roach, 1967; Adler et al., 1983). The point of T_B minimum (T_{\min}), or cold point, is usually collocated with the point of maximum height (z_{\max}). This has even been evident on a smaller scale in IR images produced from aircraft overflights (see Fig. 1), where each turret penetrating the tropopause has a cold point, and lidar-based height measurements indicate a strong cold-high correlation (Adler et al., 1983). The T_{\min} observed by GOES (with a ~ 10 km IFOV³ at midlatitudes) can be as much as 10–12 K colder than tropopause (or neutral point) temperature (Adler and Fenn, 1979; Negri and Adler, 1981; Adler et al., 1982), with severe thunderstorms typically having a lifetime GOES T_{\min} of at least 5 K colder than the tropopause temperature (Adler et al., 1985). High-resolution observations (1 km IR) indicate that the averaging effect of the 10 km GOES IFOV accounts for 3–10 K warm bias in mature overshooting thunderstorms (Adler et al., 1982), so that actual (high resolution) T_{\min} may be as much as 20 K colder than the tropopause and/or ambient temperatures at cloud top level.

In these “typical” overshooting tops, there is evidence that the effect of mixing is relatively weak and temperature–height relations are much closer to adiabatic than ambient. First, Adler et al. (1983) obtained a near adiabatic (9 K km^{-1}) cloud surface lapse rate over the overshooting top in Fig. 1 using the nadir-viewing lidar and IR radiometer on the overflight aircraft. Second, Negri (1982) has shown an 8 K km^{-1} temperature–height relation (see Fig. 2) among a collection of penetrating storms using AVHRR (1 km) T_{\min} and maximum height deduced from stereoscopic calculations from GOES-East and GOES-West. These penetrating thunderstorm tops with the high correlation (near adiabatic) between T_{\min} and height, both in the pattern of individual tops (T_B and height contours are parallel) and in a set of storms as in Fig. 2, will be termed Class 1 thunderstorm tops in this paper. A majority of storm tops fall into this category.

In a second class of penetrating storms, a cold V-shaped feature in the IR is produced with the apex of the V (with the IR cold point) pointed upwind and a relative maximum in T_B inside the V shape (Adler et al., 1981; Negri, 1982; Fujita, 1982; Heymsfield et al., 1983a,b; McCann, 1983; Mack et al., 1983). This produces a cold–warm couplet in the IR image, as shown in Fig. 3b in the southwest portion of the anvil. These close-in, cold–warm couplets have a dimension of 20–40 km, are situated primarily over the convective tops, and should not be confused with the larger anvil-scale feature of the same pattern (see Heymsfield et al., 1983a,b, for a more complete description). The general V-shaped cold feature and cold–warm couplet have been shown by McCann (1983) and Adler et al. (1985)

to be correlated with the occurrence of severe weather. Satellite stereo height patterns do not show a V-shaped or high–low couplet, but indicate instead a typical pattern of concentric height contours (see Fig. 3a). In this class (Class 2), the storm tops have a cold point nearly collocated with the high point and the warm point located in an area of downward sloping clouds downwind of the summit.

The Class 3 storm is a variation on Class 2, when, in addition to the cold–warm couplet, the cold point is offset significantly upwind from the high point, with the cold–warm couplet straddling the convective cloud top (as determined from stereo). An example of a Class 3 thunderstorm top is shown in Fig. 4. A detailed analysis of this storm complex is given by Heymsfield et al. (1983a,b), Fujita (1982), and Mack et al. (1983). In some cases, the cold V-shaped area does not have a distinct, isolated cold point, but has a relatively flat T_B pattern with multiple weak cold points.

The temperature–height contour patterns for Classes 2 and 3 are significantly different from those of Class 1. In addition, the relation of T_{\min} to z_{\max} for a collection of storms in this situation is also quite different, as seen in Fig. 5 for the storm complex on 2 May 1979, of which the thunderstorm top in Fig. 4 was a part. The data points in Fig. 5 connected by horizontal lines are storm tops with cold–high offsets. The point on the right end of the line is the T_B at the point of z_{\max} . The left hand point is the coldest T_B in the area, thus the ΔT represents the T_B difference between the cold point and the high point. The observed “lapse rate” of the collection of thunderstorm tops is near isothermal, closer to the ambient than adiabatic, indicating a larger effect of mixing than the storms in Fig. 2 (Class 1).

The three classes defined in the preceding paragraphs are not meant to be rigid, but are meant to clarify key observational characteristics and their relations to one another. A particular storm may pass from one class to another (usually from Class 1 to 2 or 3 as it matures and penetrates farther above the tropopause) and storms in close proximity may be of different classes, as is the case in Fig. 3, when the storm complex near the center of the panels has parallel height and T_B contours (Class 1), while the storm to the southwest is a Class 2 example.

The causes for the IR V-shaped cold feature and imbedded warm point of classes 2 and 3 have been discussed by Heymsfield et al. (1983a,b) and Fujita (1982). Heymsfield pointed out that the warm point sometimes is located close-in to the cold point or apex of the cold V with a cold–warm separation of ~ 40 km, as mentioned in the Class 2 description before. Additionally, another warm point can occur much farther downwind, about 100 km from the cold point. These two points may exist at the same time (as in Heymsfield’s case study) and probably have different causes. The large-scale (anvil-scale), V-shaped cold area with the downwind (100 km) warm point is probably related

³ Instantaneous Field Of View.

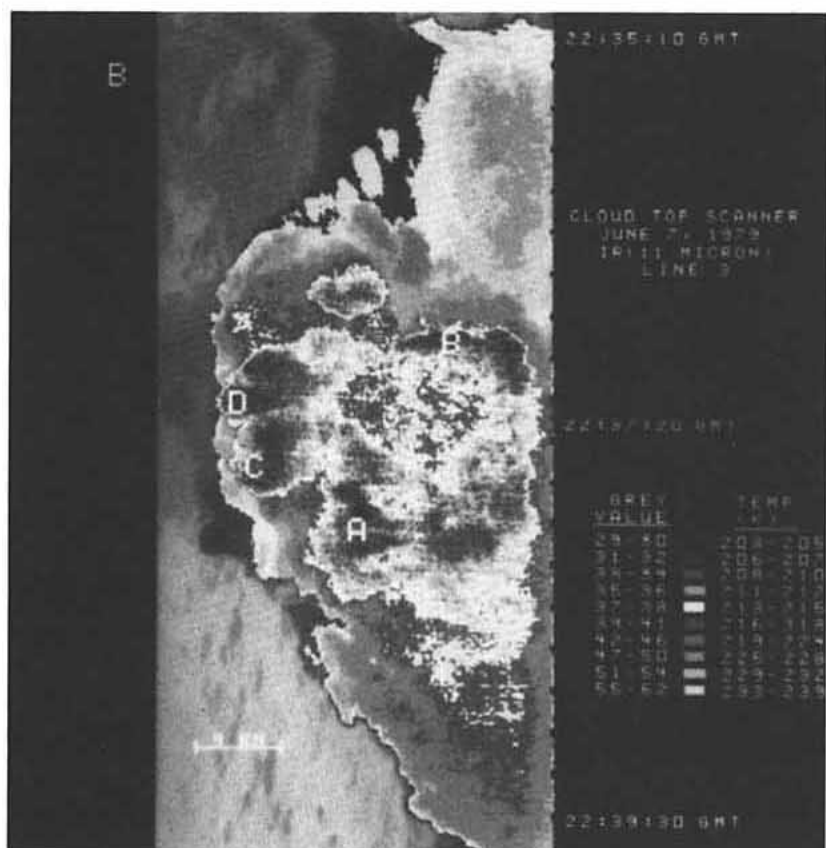


FIG. 1. A visible and infrared view from an aircraft of a "typical" penetrating thunderstorm with monotonic T_B -height patterns. Adapted from Adler et al. (1983).

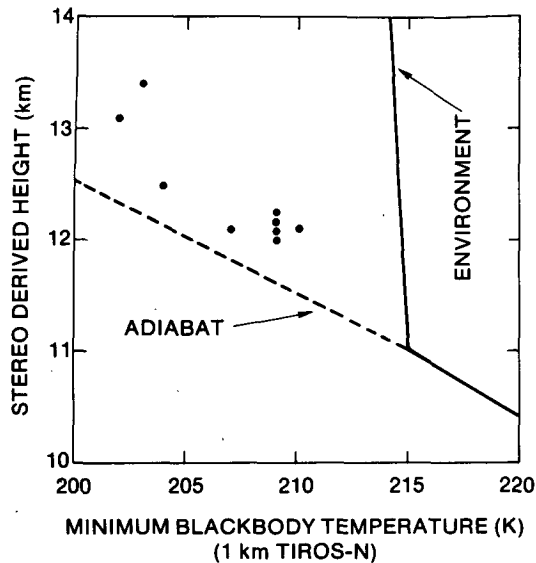


FIG. 2. IR brightness temperature–maximum height for a collection of nine storms on 10 April 1979. Adapted from Negri (1982).

to the distribution of Ice Water Content (IWC) in the anvil and its effects on the upwelling radiance (Heymsfield et al., 1983b). The lower IWC in the central part

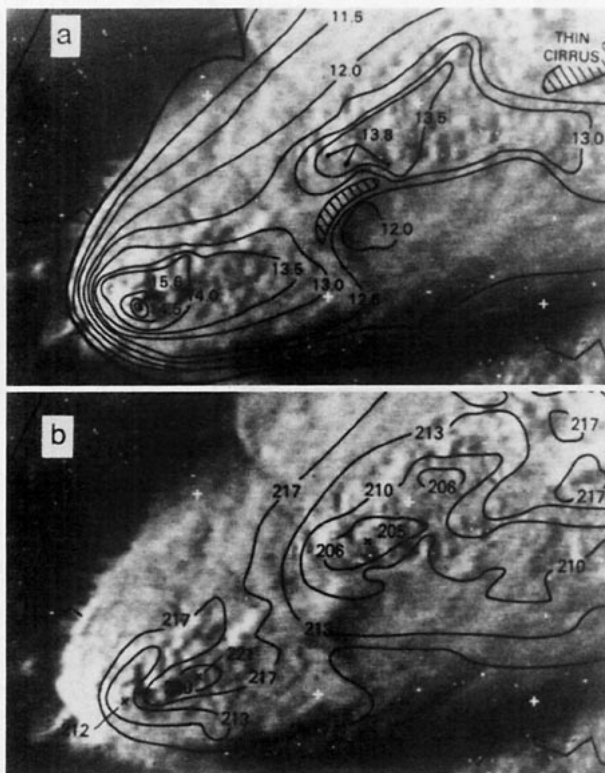


FIG. 3. Stereoscopic height contours (a) and GOES IR T_B contours (b) for the Wichita Falls, Texas, 10 April 1979 storm (southwest end of anvil) overlain on the GOES-East visible image.

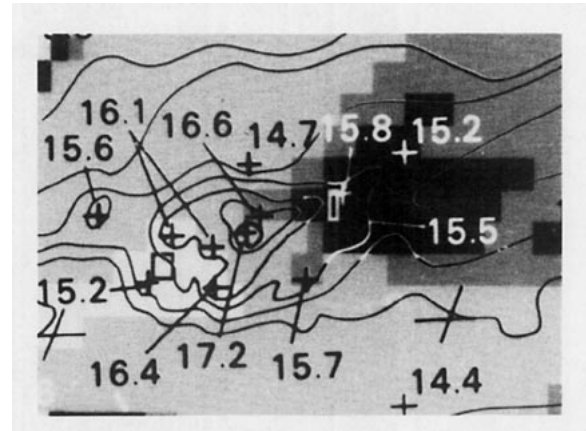


FIG. 4. An IR image of a thunderstorm top overlain with stereo height contours on 2 May 1979. The white area has low T_B with the boxed point having a T_{\min} of 199 K, while the boxed point in the black area is at 215 K. The distance between the cold and warm points is ~ 35 km. Adapted from Mack et al. (1983).

of the anvil, where the warm point is, as compared to the larger IWC in areas of the cold V, produces warmer T_B , even though the anvil top is roughly at the same altitude across both the cold areas and the warm point. An alternate hypothesis for the warm point is the presence of above-anvil cirrus in the stratosphere radiating at temperatures warmer than the anvil background and producing the interior warm point (Fujita, 1982).

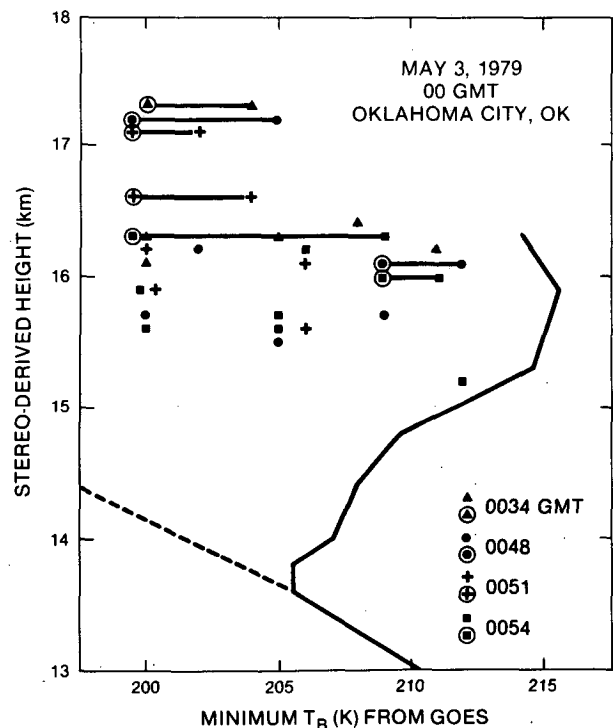


FIG. 5. Observed GOES T_{\min} –stereo z_{\max} for a collection of storm tops on 2 May 1979. This figure is similar to those of Hasler (1981) and Fujita (1982).

The close-in warm point (40 km) may be related to the dynamics of the overshooting top itself and its interaction with the lower stratosphere (Heymsfield et al., 1983a), where the warm point is related to subsidence in the convection region and mixing with the stratospheric environment. Schlesinger (1984) has used a three-dimensional cloud model to simulate the temperature and height pattern at cloud top in an intense storm in a high-shear environment and the resulting patterns are shown in Fig. 6. The model produces the cold-warm couplet (only 12 km apart) with the high point just slightly upwind of the cold point and the warm point on the sloping cloud surface downwind of the cold-high point. These model results support the dynamic cause for the close-in feature. An alternate hypothesis for the close-in warm point is that of the above-anvil cirrus (Fujita, 1982), in which cirrus debris in the lower stratosphere overlays the convective top and produces warm values of T_B . The cold-high offset of the Class 3 storms would thus be the result of the cirrus covering up the point of z_{\max} and forcing the lowest T_B value to be located upwind, where the cirrus debris does not cover the convective top.

The actual cause of the Class 2 and 3 features (V-shaped cold area, cold-warm couplet) is still not proven and may be a combination of the factors discussed before. This current paper centers on exploring the dynamic explanation for the close-in, cold-warm couplet, and convective top structure and T_B - z relations for all three classes of storms. The approach is to use a simple, one-dimensional parcel model to duplicate parcel trajectories in temperature-height space above the neutral

point in the overshooting region under a variety of environmental and in-storm conditions. These model results will then be compared to the satellite and aircraft observations already described and to Schlesinger's three-dimensional model results.

The existence of cirrus debris at altitudes higher than the main anvil has been inferred from satellite imagery (Fujita, 1982) and observed from aircraft (Adler et al., 1983; Spinhirne et al., 1983). The origin of this above-anvil cirrus debris or of elevated areas of the anvil itself and their possible relation to the T_B warm areas in the satellite IR imagery will also be discussed in relation to the model results.

3. Parcel model description

The vertical equation of motion appropriate for cloud-scale dynamics given by Schlesinger (1980, 1984) is

$$\frac{dw}{dt} = -\frac{1}{\rho_0} \frac{\partial p'}{\partial z} + g \left(\frac{\theta'}{\theta_0} + a q'_v \right) - g \frac{C_v p'}{C_p p_0} - g q_l + F_z, \quad (1)$$

where

- w vertical velocity,
- ρ air density,
- p pressure,
- z height,
- g gravity,
- θ potential temperature,
- a $[=R_v/R_d - 1 (\approx 0.606)]$,
- R_d gas constant for dry air,

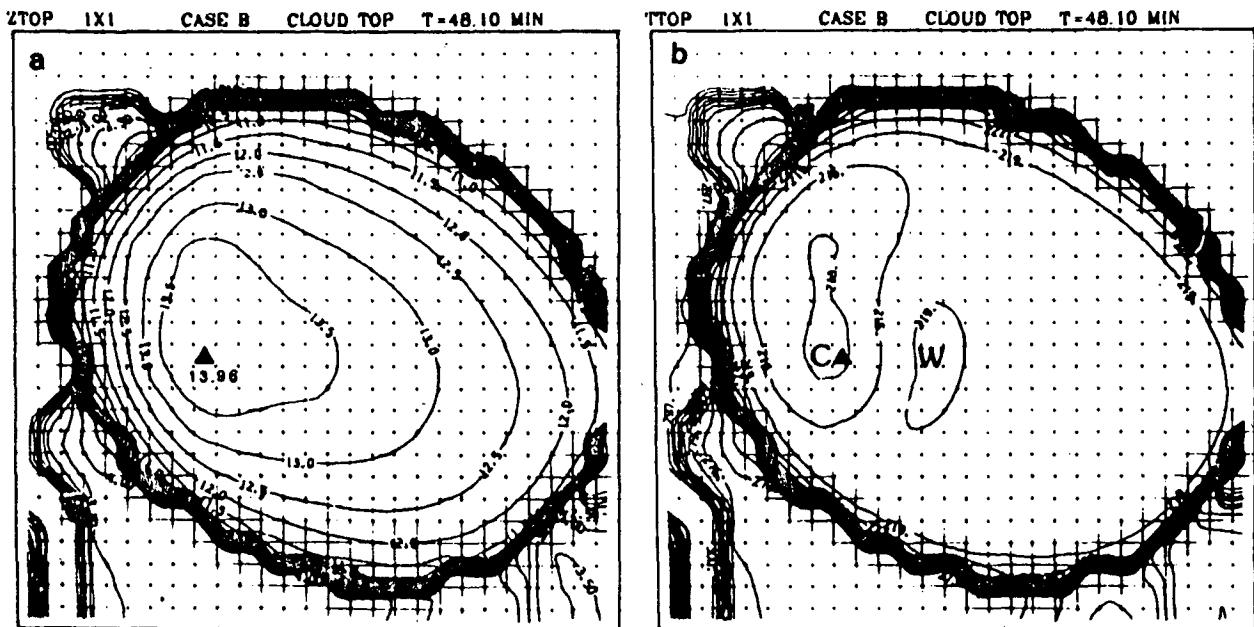


FIG. 6. Three-dimensional cloud model results, showing temperature and height patterns at the top of a mature, overshooting thunderstorm. Adapted from Schlesinger (1984).

- R_v gas constant for water vapor,
 q_v water vapor mixing ratio,
 C_p specific heat of dry air at constant pressure,
 C_v specific heat of dry air at constant volume,
 q_l liquid water mixing ratio,
 t time,
 F_z vertical component of the friction force.

The individual terms on the right-hand side are, from left to right: the perturbed vertical pressure gradient force which tends to oppose the thermal buoyancy; the moist thermal buoyancy which accelerates an air parcel upward if it is warmer or more moist than its surroundings; the pressure buoyancy which will accelerate an air parcel upward if it is at lower pressure than its surroundings; the liquid water drag and, finally, the vertical friction (turbulent diffusion of vertical momentum).

In our one-dimensional parcel (or Lagrangian) model, the pressure perturbation terms cannot be calculated directly, but are parameterized as a function of thermal buoyancy. This formulation is given by

$$\frac{dw}{dt} = \frac{\alpha g(T - T_e)}{T_e} - gq_l - \mu_w |w|w, \quad (2)$$

where

- T cloud parcel temperature,
 T_e environmental temperature,
 α pressure perturbation coefficient,
 μ_w vertical momentum mixing coefficient.

The first term on the right-hand side of Eq. (2) is a rough approximation to the combination of the thermal buoyancy force and the effect of the two pressure perturbation terms. The effect of moisture on the buoyancy is ignored because moisture is negligible in the upper troposphere and lower stratosphere. The pressure perturbation coefficient, α , is used in Eq. (2) to parameterize the pressure gradient and pressure buoyancy terms in Eq. (1), i.e.,

$$\frac{\alpha g(T - T_e)}{T_e} = g \left(\frac{\theta'}{\theta_0} \right) - \frac{1}{\rho_0} \frac{\partial p'}{\partial z} - g \frac{C_v}{C_p} \left(\frac{p'}{p_0} \right). \quad (3)$$

The basis of this parameterization is as follows: Holton (1973) indicated that the perturbation pressure gradient force tends to oppose the thermal buoyancy and this is clearly indicated in three-dimensional cloud model results [see Fig. 4 in Schlesinger (1980)]. Although much smaller in magnitude than the perturbation pressure gradient term, the pressure buoyancy [last term in Eq. (3)] also opposes the thermal buoyancy in the overshooting region. In the troposphere, the thermal-pressure buoyancy relation is not as clear, but the pressure buoyancy magnitude is small (Schlesinger, 1980). The three-dimensional cloud model results also indicate that the perturbation pressure gradient force is larger relative to the thermal buoyancy in the overshooting (stratosphere) region than it is in the tropo-

sphere. These relations between the thermal buoyancy and the perturbation pressure terms are not well understood and require further investigation.

In this study, it is assumed that the combined perturbation pressure terms are correlated with the thermal buoyancy and oppose it. This results in a reduced buoyancy similar in effect to the use of an apparent mass coefficient (Simpson and Wiggert, 1969), although the physical basis is completely different. The magnitude of α near the cloud top was selected based on an analysis of three-dimensional cloud model parcel trajectories from Schlesinger (1984). The magnitude of the terms on the right-hand side of Eq. (3) was determined at various heights from parcels (KM1, LM2) in the Schlesinger study. These parcels originated in the low-level warm moist layer, were swept through the updraft core, through the cold area, into the stratosphere, and then finally downward into the warm area. The sum of these three terms at various heights along the parcels' path near the cloud top are plotted versus the thermal buoyancy in Fig. 7. A regression line was fit to the points and a correlation coefficient of 0.87 was found. The regression line has a slope of 0.2 and an intercept of near zero. This indicates that the pressure gradient and pressure buoyancy forces at cloud top act to significantly counteract the thermal buoyancy term (B) so that the combined "buoyancy" (B') is approximately one-fifth the thermal buoyancy ($\alpha \approx 0.2$ in Eq. 2). In the model runs to follow, α will be manipulated to produce model cloud top heights comparable to observations.

The ice water drag term (the weight of the ice) in Eq. (2) will be varied for an acceptable range that has been observed near thunderstorm cloud tops. The final magnitude will then be determined from results that best simulate observations.

The final term in Eq. (2), the momentum mixing term, is determined by the parcels' vertical velocity

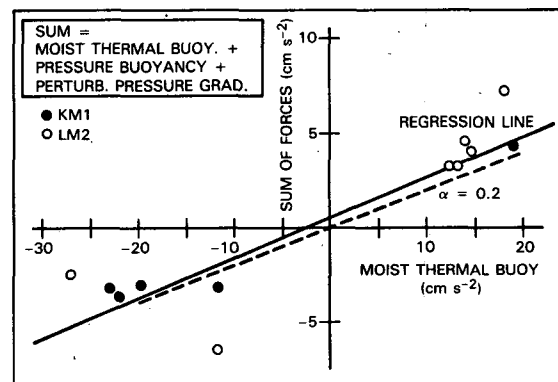


FIG. 7. Sum of pressure perturbation terms and temperature buoyancy term as a function of temperature buoyancy term. Adapted from results from Schlesinger (1984) for parcel trajectories in the overshooting region of a model thunderstorm. A $\alpha = 0.2$ line compares well with the line fitted through the model calculation.

and a momentum mixing coefficient, μ_w . The mixing coefficient is varied in order to study the effects on the path of the parcel caused by the amount of mixing.

To solve for the parcel temperature (T) in Eq. (2), the following relation is used:

$$\frac{dT}{dt} = -w(g/c_p) - |w|\mu_T(T - T_e), \quad (4)$$

where μ_T is the thermal mixing coefficient and is set equal to $3\mu_w$, similar to three-dimensional model work. The first term on the right-hand side of Eq. (4) represents the rate of change of temperature a parcel would experience if it ascends dry adiabatically. The second term represents the effect on the parcel's temperature due to mixing with the environment.

A fourth-order Runge-Kutta numerical scheme with a 5 s time step was used to solve simultaneously Eqs. (2) and (4), thus calculating a parcel trajectory in T and Z space. Vertical acceleration is assumed to be constant between time steps.

The one-dimensional parcel model is initiated by starting a parcel at the neutral point with w set equal to some initial value, w_0 , parcel temperature (T) set equal to the environmental temperature (T_e), and a specified environmental temperature profile above the neutral point. Using different lapse rates, mixing, w_0 , and drag, attempts are made to simulate cloud top dynamics and structure and to determine the importance of various factors producing observed features.

4. Results of basic model runs

The cloud-top parcel model was run with a variety of values of the pertinent variables to simulate the effect of different environmental conditions (lapse rate, mixing) and different cloud conditions (w_0 , drag). With reasonable ranges of the variables, it was attempted to reproduce the observations discussed in section 2. For most of the modeling runs, α was set equal to 0.15, meaning that the sum of the pressure perturbation and buoyancy terms is set equal to 15% of the thermal buoyancy, i.e., $B' = 0.15B$. This is a slightly smaller α than was indicated by the analysis of the Schlesinger model trajectories in the previous section. The slightly smaller value was used because it produced maximum height values closer to observed values. The drag term does not vary during the model run and is initially set to 0.02 m s^{-2} , which is equivalent to an ice water concentration (IWC) of $\sim 0.4 \text{ g m}^{-3}$. This is reasonable in the overshooting top region of a large thunderstorm. The magnitude of the drag term is later varied to determine its effect on the simulated parcel path. The range of the mixing parameters ($\mu_T = 0.3\text{--}1.0 \text{ km}^{-1}$) was chosen based partly on experience with other one-dimensional models (Simpson and Wiggert, 1969; Adler and Mack, 1984) and comparisons of the model temperature-height relations with observations.

This simple model attempts to reproduce the parcel

path in temperature-height space for a parcel ascending through the updraft core to the top of the overshooting dome and then descending the downwind side of the dome. The model parcels are initiated at the near-tropopause neutral thermal buoyancy point with a selected initial vertical velocity, w_0 . Figure 8 gives a synopsis of parcel runs with an isothermal stratosphere, with Fig. 8a having $\mu_T = 0.3 \text{ km}^{-1}$ and Fig. 8b having $\mu_T = 1.0 \text{ km}^{-1}$. The variation in mixing as parameterized by variations in μ_T and μ_w represents differences in cloud top-environment interactions, which may be a function of the magnitude of the vertical shear at cloud top.

In Fig. 8a, three model runs are shown. Both start at the same neutral point at 13.6 km and 204 K (a point which is arbitrary for these runs, but has relevance to the 2 May 1979 case). Because every variable is identical except the w_0 in the three runs, all runs initially

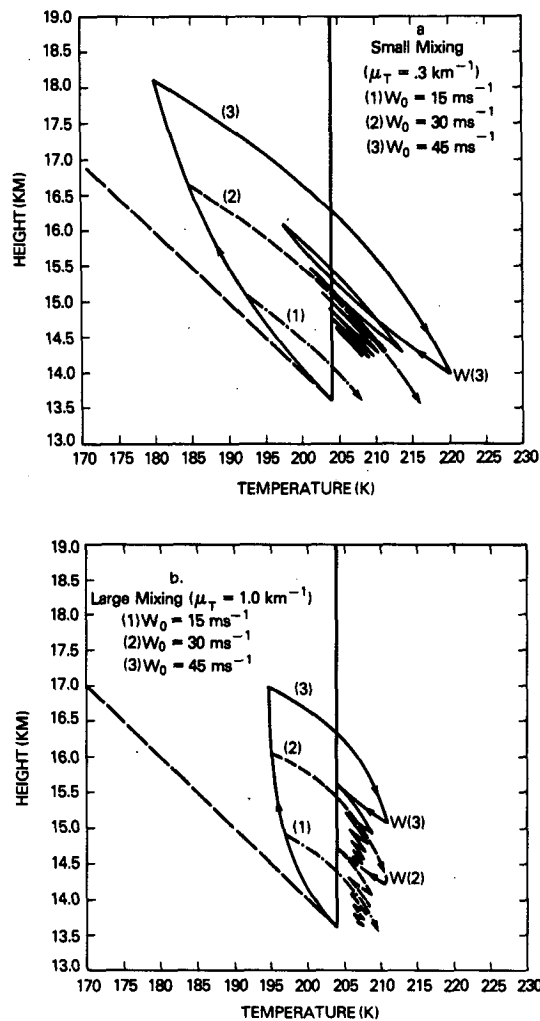


FIG. 8. Parcel model trajectory results for an isothermal stratosphere and (a) small mixing: $\mu_T = 0.3 \text{ km}^{-1}$ and (b) large mixing: $\mu_T = 1.0 \text{ km}^{-1}$. In both cases, $\alpha = 0.15$ and drag is 0.02 m s^{-2} .

have the same parcel path, up to 15.0 km where run (1), with $w_0 = 15 \text{ m s}^{-1}$, reaches its maximum height and begins to descend as shown. Runs 2 and 3 with $w_0 = 30$ and 45 m s^{-1} ascend farther to 16.6 and 18.1 km. As expected by Newton (1966), the descending portion of the parcel path is at temperatures significantly warmer than those of the ascending path due to the mixing. This temperature–height path taken by the descending parcel on the periphery of the dome should be the best match with the observed T_B –height path obtained by aircraft overflights of storm turrets (e.g., Adler et al., 1983). In Fig. 8b, the same runs are shown for large mixing ($\mu_T = 1.0 \text{ km}^{-1}$). The larger mixing obviously tends to pull the parcel trace toward the ambient lapse rate and produces lower maximum heights and higher T_{\min} values for the same w_0 values as in Fig. 8a.

In all parcel runs displayed in Fig. 8, the cold point is collocated with the high point. An examination of the model equations indicates that in our simple system the parcel trajectories can only be between adiabatic and environmental lapse rates (on the way up), so that for an isothermal stratosphere or a lapse of temperature with height no cold–high offset can occur. On the descent side of the parcel trajectory in Figs. 8a and 8b, some interesting features are apparent. For the small mixing (Fig. 8a), runs 1 and 2 ($w_0 = 15$ and 30 m s^{-1} , respectively) show parcels descending through the neutral point height (13.6 km) without having a point of relative maximum of temperature. For run 3 in Fig. 8a ($w_0 = 45 \text{ m s}^{-1}$), a warm point (W) is created by the positive B' force (combination of thermal buoyancy and pressure perturbation terms) counteracting the downward momentum and drag. The parcel then goes through large oscillations and gradually descends on the warm side of the ambient lapse rate due to the effect of the drag term.

With the small mixing, this warm/low point and attendant oscillations occur only with a parcel reaching nearly unreasonable heights ($>4 \text{ km}$ tropopause penetration). With larger mixing (Fig. 8b), the effect occurs with updrafts penetrating about 2.5 km above the neutral point. The model runs indicate that the occurrence of the warm point is associated with storms with significant penetration above the neutral point and having intense mixing occurring at cloud top.

The warm point itself, which in Fig. 8b is 5 K warmer than the environment, is caused by the overshooting of the ambient temperature on the downward path. Thus, the cause is primarily dynamic and not radiative (e.g., due to emissivity variations). The following oscillations may be interpreted as cirrus debris coming off the convective turrets, floating downwind, and slowly reaching equilibrium at heights significantly above the neutral point height. One inconsistency still exists in relation to the warm point. The model results in Fig. 8 have the warm point occurring at a low point,

not in a downward-sloping cloud as deduced from the satellite observations. This will be explored further in a following section.

In summary, model runs 1 and 2 in Fig. 8a represent Class 1 storms as described in the following section. Model runs 2 and 3 of Fig. 8b are possible candidates for simulating some of the key features of the Class 2 storm.

Figure 9 shows a summary of the temperature and height at the parcel peak height for the isothermal runs. The distribution for the small mixing has a temperature height relation of $\sim 7 \text{ K km}^{-1}$ in the first 2 km above the neutral point, similar to observations as in Fig. 2.

Figure 10 gives the model results for a 4 K km^{-1} inversion, similar to that observed with the 2 May 1979 case discussed in the observations. The starting neutral point is realistic for that case also. The first parcel (Fig. 10a), for small mixing, is similar to the results for the isothermal situation, except the parcel tracks on the upward path are farther from adiabatic because of the greater distance of the environmental lapse rate from adiabatic. These model runs also appear similar to parcel trajectories schematically drawn by Danielsen (1982) to explain observed anvil vertical temperature distributions by relating them to mixing of ascending and descending air in overshooting tops resulting in a near-adiabatic layer of intermediate potential temperature in the anvil.

For the large ($\mu_T = 1.0 \text{ km}^{-1}$) mixing, the stratospheric inversion begins to produce cold–high offsets (Fig. 10b). Also, downside warm points and the associated oscillations are produced for parcel runs penetrating to reasonable heights (16 km). The model run for 15 m s^{-1} in Fig. 10b still has a collocated cold and high point. However, in the 30 and 45 m s^{-1} runs in

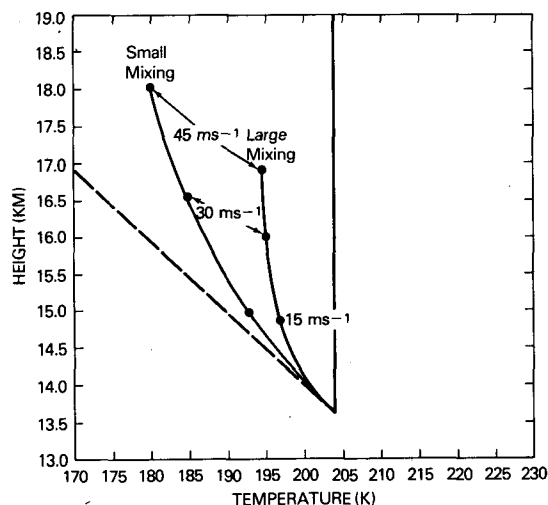


FIG. 9. Summary of maximum height–minimum temperature model results for isothermal stratosphere for various mixing coefficients.

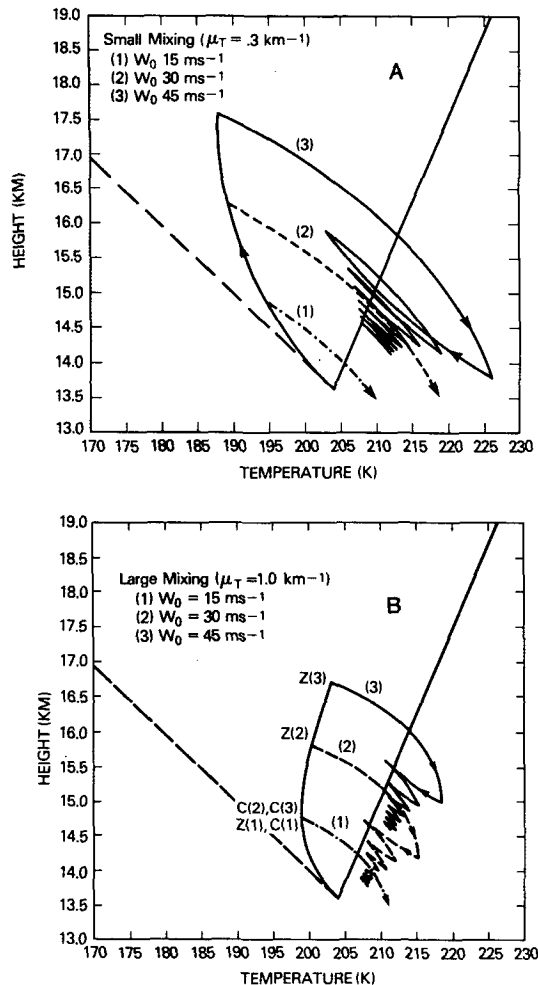


FIG. 10. Parcel model trajectory results for a 4 K km^{-1} inversion and (a) small mixing, $\mu_T = 0.3 \text{ km}^{-1}$; (b) large mixing, $\mu_T = 1.0 \text{ km}^{-1}$. In all cases, $\alpha = 0.15$ and drag is 0.02 m s^{-2} .

Fig. 10b, the coldest point (C) of the run is achieved at 14.8 km, prior to the maximum height. The occurrence of this cold-high offset in the model is due to the strong inversion, large mixing, and strong updraft. The cold point-warm point temperature difference of $\sim 18 \text{ K}$ in run 3 in Fig. 10b is approximately in agreement with observations (see section 2). Again (as in Fig. 8b), the warm point is related to the overshooting of the ambient temperature on the downward path and the following oscillations may be related to the downwind cirrus which is sometimes observed. Figure 11 summarizes the minimum temperature-maximum heights of the model runs for the small and large mixing, with the points connected by curves being the temperatures at the maximum height and the circled points offset toward lower temperature being the T_{\min} , where there is a cold-high offset. The general isothermal distribution for the large mixing, the occurrence

of cold-high offsets for storms at higher heights, and the increase of the temperature offset as a function of height agree, at least qualitatively, with the plotted observations of Fig. 5.

One of the keys points concerning the warm point is related to the effect of drag on the air parcel. Figure 12 shows three model runs with identical parameters as run 3 in Fig. 10b except for values of drag = 0.03, 0.045 and 0.06 m s^{-2} . With increasing drag, maximum height obtained by the parcel decreases, but more importantly, there are significant differences in the warm point. In Fig. 12a, with a drag of 0.03 m s^{-2} , the result is basically the same as with 0.02 m s^{-2} in run 3 of Fig. 10b. That is, the warm point, W, is located at a low point and is followed by large height and temperature oscillations, but with a general trend of decreasing height.

As the drag increases (Figs. 12b and 12c), the downward parcel creates a warm point (W), not at a low point, but at a point where the parcel is still descending. In Fig. 12b, the warm point is followed by the same type of oscillations previously noted, but now with smaller height and temperature displacements. For the largest drag (Fig. 12c), the parcel descends through the neutral point before decelerating to 0 m s^{-1} so that no oscillations appear. The model runs in Figs. 12b and 12c with the warm point (W) located on a downward path may be simulating the observed feature of the warm point being located on a downward-sloping cloud surface. The maximum temperature relations point to the model runs of Figs. 12a-c being simulations of the features of Class 3 storms.

Figures 13 and 14 summarize the effect of differing lapse rates on the cold (C) and warm (W) points for

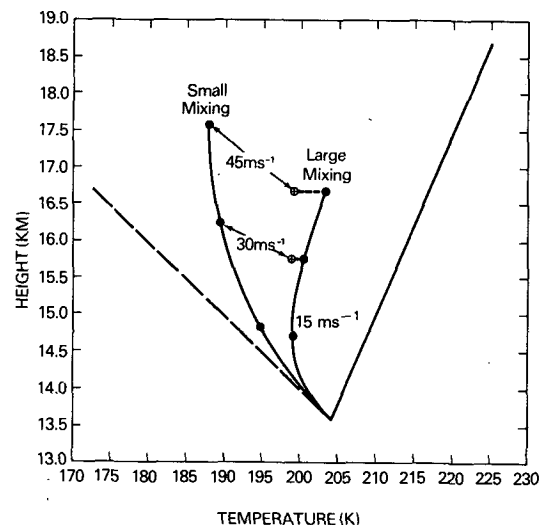


FIG. 11. Summary maximum height-minimum temperature model results for 4 K km^{-1} inversion for various mixing coefficients.

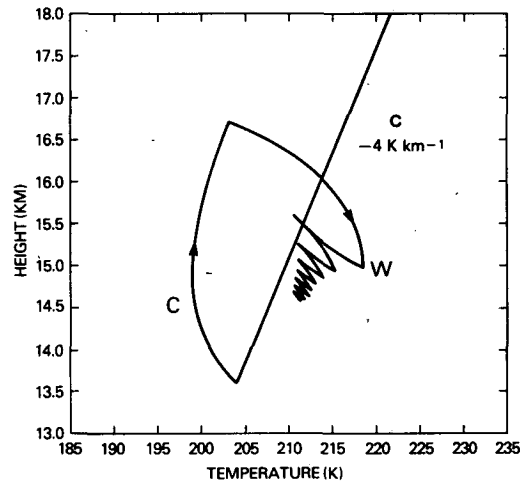
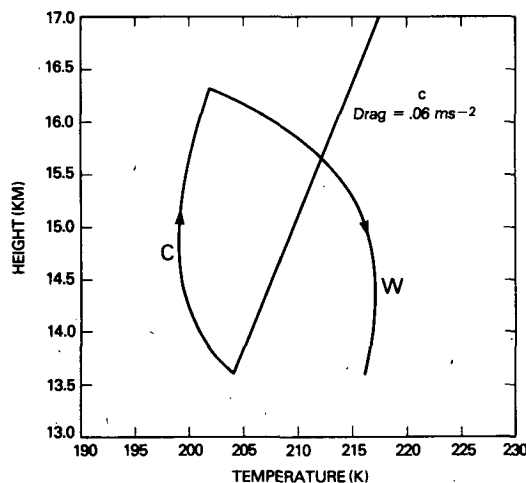
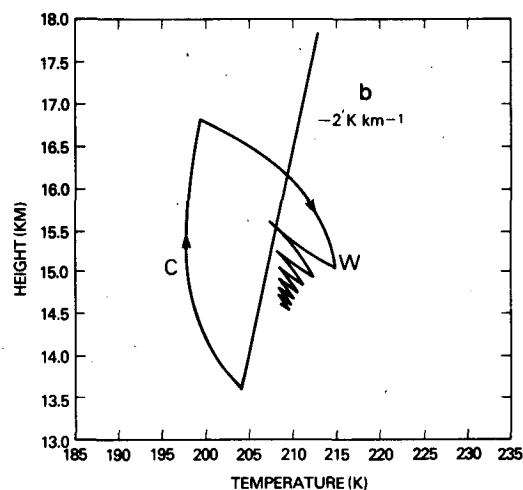
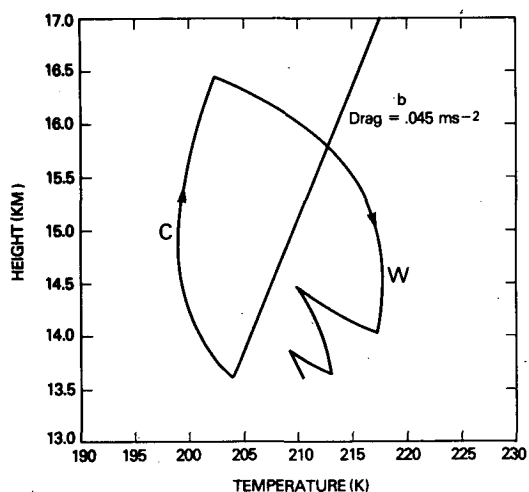
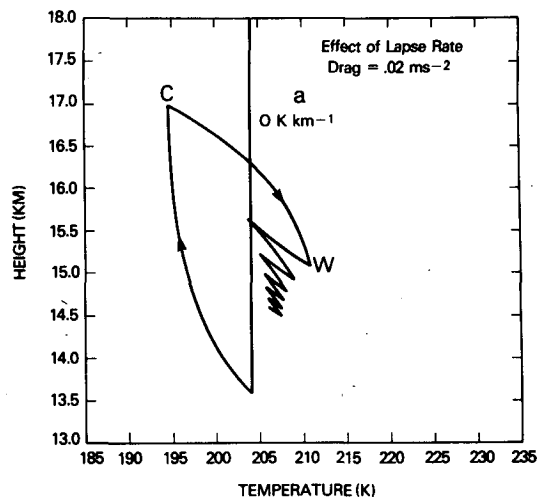
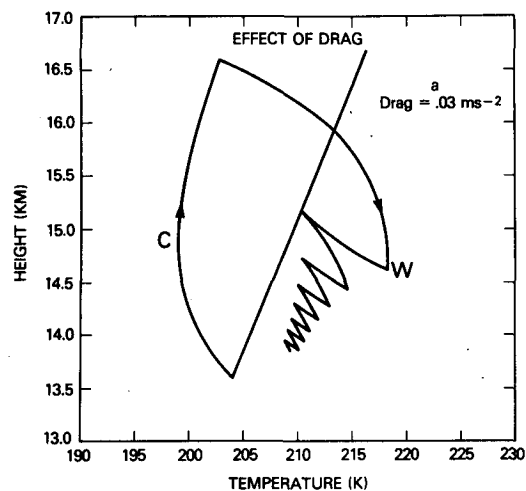
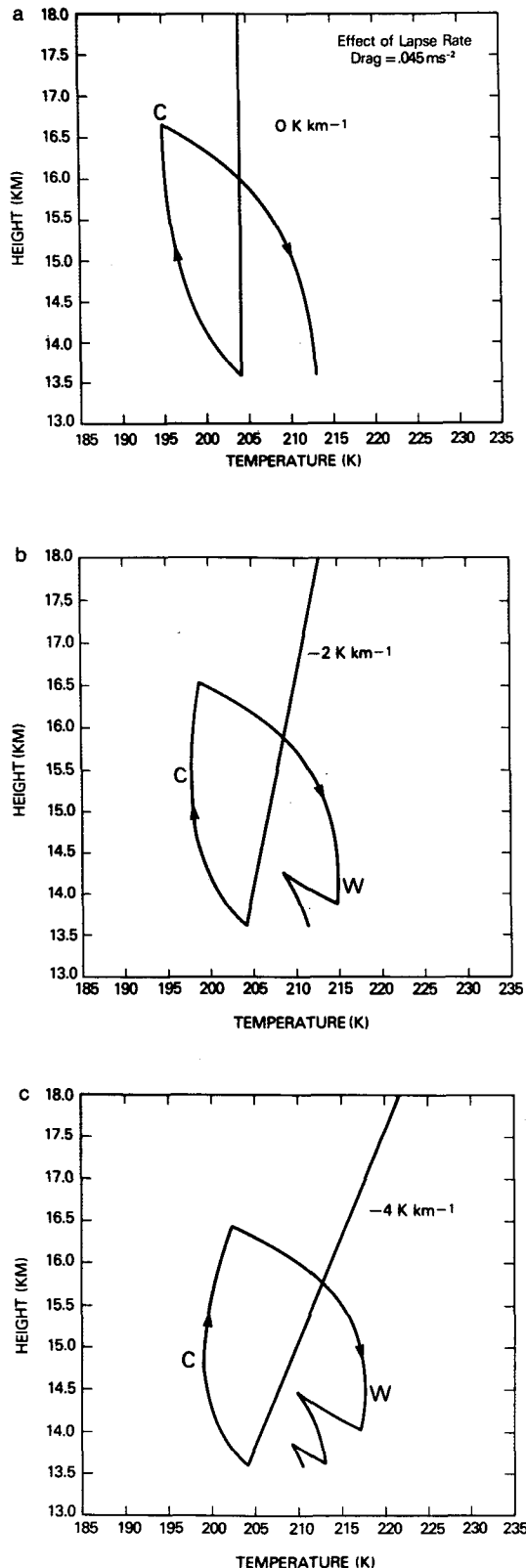


FIG. 12. Parcel model results showing effect of different values of drag. Lapse rate is -4 K km^{-1} , $\alpha = 0.15$, and $\mu_T = 1.0 \text{ km}^{-1}$. Drag is (a) 0.03 m s^{-2} , (b) 0.045 m s^{-2} and (c) 0.06 m s^{-2} .

FIG. 13. Parcel model results showing effect of lapse rate with drag $= 0.02 \text{ m s}^{-2}$, $\alpha = 0.15$, and $\mu_T = 1.0 \text{ km}^{-1}$. Lapse rate is (a) 0.0 K km^{-1} , (b) -2 K km^{-1} and (c) -4 K km^{-1} .

FIG. 14. As in Fig. 13 but drag is 0.045 m s^{-2} .

two values of drag. In both Figs. 13 and 14, the cold point is collocated with the high point for isothermal conditions. As the inversion intensity is increased (in both Figs. 13 and 14), the cold point becomes offset from the high point with the amount of offset in terms of height or temperature being directly related to the inversion strength. For a small drag (Fig. 13), the height of the warm point (located at a low point) is not substantially affected by the lapse. For a larger drag (Fig. 14), the existence and the height of the warm point are functions of the lapse rates with the warm point moving higher for stronger inversions.

Figure 15 summarizes schematically the three classes of storm tops and the possible trajectory of the updraft core air associated with each. For Class 1, the key ingredient is that the effect of mixing is small so that the parcel trajectory in temperature–height space is closer to adiabatic than ambient. The cloud top cross section for Class 1 indicates that the cloud surface temperature and height (e.g., as observed by aircraft by Adler et al., 1983) are associated with the descending leg of the trajectory.

For Classes 2 and 3, the key ingredient is large mixing, which is related to the vertical shear in the cloud top region. For storm tops under conditions of large mixing but with small vertical velocities and small height penetrations above the neutral point, the temperature–height patterns will be similar to those storm tops occurring under conditions of small mixing. However, with larger vertical velocities and larger stratospheric penetrations, large mixing leads to the occurrence of cold–warm couplets. Indeed, Schlesinger (1984) indicated that the strength of the cold–warm couplet is related to the magnitude of the shear in the near-tropopause region. The main difference observationally between Classes 2 and 3 is the collocation of the cold–high point (Class 2) or the upwind offset of the cold point from the high point (Class 3). As indicated in the previous model runs, and schematically in Fig. 15, this difference is related to the strength of the inversion. The warm point located at a low point (in Class 2) does not fit with observations, but may indicate a limitation of the model or the stereoscopic analysis.

The oscillations following the warm point indicate parcels gradually approaching thermal equilibrium at an altitude significantly above the tropopause. This is interpreted in the schematic as an elevated anvil downwind of the convective core. A slightly different interpretation would have the cloud top trajectory associated with a layer of thin cirrus above the main anvil layer, the above-anvil cirrus postulated by Fujita (1982). The actual warm point is, however, placed at a location indicating that the subsidence dynamics is the main effect creating the distinct warm point. Cirrus debris further downwind may contribute to the general warm area downwind of the distinct warm point.

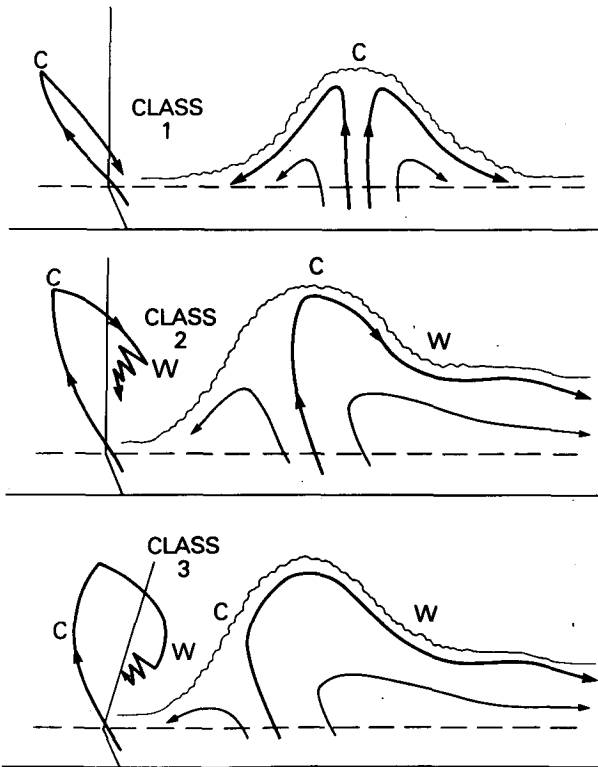


FIG. 15. Schematic of updraft parcel paths based on model results and cross sections of storm tops illustrating the three classes of storm tops.

5. Simulation of the 2 May and 10 April 1979 storms

In this section, the model is manipulated in an attempt to reproduce the major height and temperature characteristics of the 2 May 1979 storm in Fig. 4 and the Wichita Falls, Texas, storm of 10 April 1979 (Fig. 3). It should be remembered in the following results that the GOES T_{\min} values are overestimates of actual thunderstorm top T_{\min} by 3–10 K for mature storms due to the coarse IFOV of GOES (Adler et al., 1982). The model T_{\min} values should, therefore, be expected to be 3–10 K lower than the comparable GOES T_{\min} values. The model-produced warm point temperature should correspondingly be slightly higher than the GOES T_B warm point.

For the 2 May case, the ambient sounding was chosen as the heavy, solid line in Fig. 16 to approximate the local conditions based on two nearby soundings. Above 16.3 km, where the sounding data stops, the inversion is assumed to weaken.

The type of features we are trying to simulate with the model in this section are similar to those produced by model run 3 in Fig. 10b with its cold-high offset and with the runs in Figs. 12b and 12c with their downslope warm point. However, in order to make comparisons quantitatively with the IR T_B and stereo

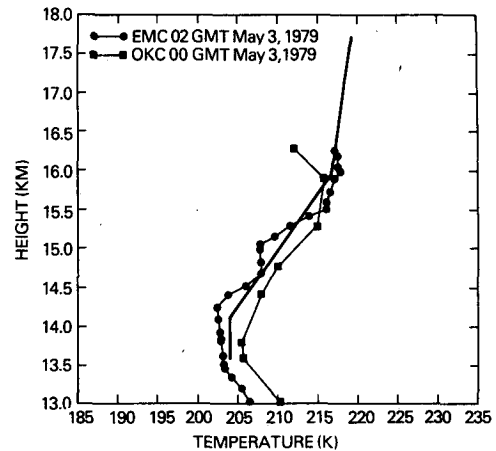


FIG. 16. Soundings associated with 2 May 1979 case and assumed soundings for model runs (solid line, no points).

height patterns in Fig. 4, a larger maximum height had to be obtained. Because 45 m s^{-1} was considered to be a reasonable upper limit to the initial vertical velocity (w_0), the additional height was obtained by decreasing the parameter α (thereby reducing the magnitude of the effective negative buoyancy). This reduction in effective buoyancy allows the negatively buoyant parcels to ascend to greater heights. With $\alpha = 0.075$ (meaning that the effective buoyancy is only 7.5% of the original buoyancy) and a w_0 of 45 m s^{-1} , a maximum height of 17.2 km was obtained (Fig. 17) along with a large cold-high offset, and a warm point, W, at 15.3 km on the downward path of the parcel trajectory. This run is similar to that in Fig. 12b, except for the larger maximum height. On the downward portion of the path, the parcel overshoots the ambient sounding, reaching

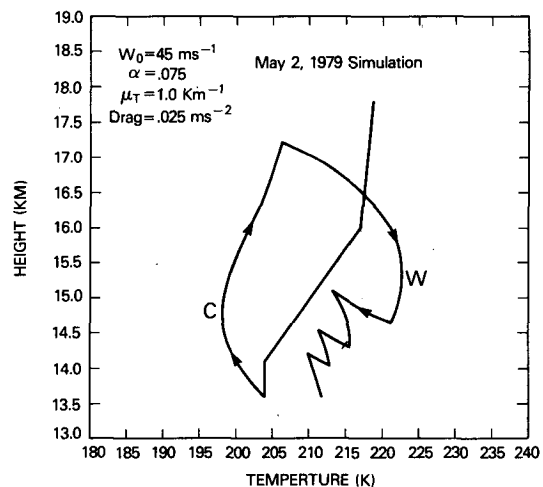


FIG. 17. Parcel model results simulating 2 May 1979 case (Fig. 4). Tick mark at 14.3 km denotes end of time plot in Fig. 18a.

a warm point, W, at 15.3 km. After the warm point on the downward slope is produced by the mixing "pulling" the trajectory back toward the ambient sounding, the parcel continues to descend until the effective buoyancy becomes larger than the drag, the parcel decelerates and stops (in terms of vertical motion), and the parcel begins to rise and cool at a rate which is a combination of adiabatic plus the mixing effect. The oscillations below 15 km in Fig. 17 represent the fluctuations of primarily the effective buoyancy against the drag in the vertical momentum equation and the temperature mixing modifying the adiabatic warming or cooling in the temperature equation. Without the effect of the drag, the parcel would oscillate about the ambient soundings.

Figure 18a shows the time plots of parcel temperature and height for the model run in Fig. 17. The time location of key points (cold point, maximum height point, warm point), along with neutral point height and temperature (z_0 , T_0), are also shown. The end point of the 1800 s time interval shown in Fig. 18a is shown as a tick mark at 14.3 km in Fig. 17. Since we are interpreting the parcel model runs as following a parcel in the updraft core reaching cloud top surface at the cold point and then continuing downwind through the high point and warm point, the time section in Fig. 18a can be thought of as a distance cross section of cloud top, if steady state conditions are assumed. The observed cross section is shown in Fig. 18b and is constructed from Fig. 4 on a line through the IR cold and warm points. The horizontal spatial scale in Fig. 18b has been set so that the positions and separation distance between the cold and warm points match those in Fig. 18a. This results in a necessary average horizontal velocity of 62 m s^{-1} . This magnitude of velocity is not unreasonable considering tropopause ambient flow of up to 50 m s^{-1} and divergent flow velocities of 60 m s^{-1} downwind of the cold point at 12 km (Fig. 5; Heymsfield et al., 1983a). Also, Lemon and Burgess (1980) note anvil-level horizontal peak velocities of well over 60 m s^{-1} for two storms observed with single Doppler radar.

The two parts of Fig. 18 have many similarities in terms of the absolute magnitudes of temperature, height, and relative positions of features. The cold point (C) is located to the left or upwind of the high point (z_{\max}) at an altitude near 15 km (only 1.5 km above the neutral point). The warm point (W) is clearly located on the downward slope (not at a height minimum) downwind of the high point. The high point (z_{\max}) is located nearly midway between the cold and warm points in a region of small horizontal temperature gradient. This small temperature gradient is due (in the model run) to the vertical velocity being near zero (see Eq. 4). A similar feature is apparent in Fig. 18b (observations). This similarity between the model and observations in terms of the small horizontal T_B

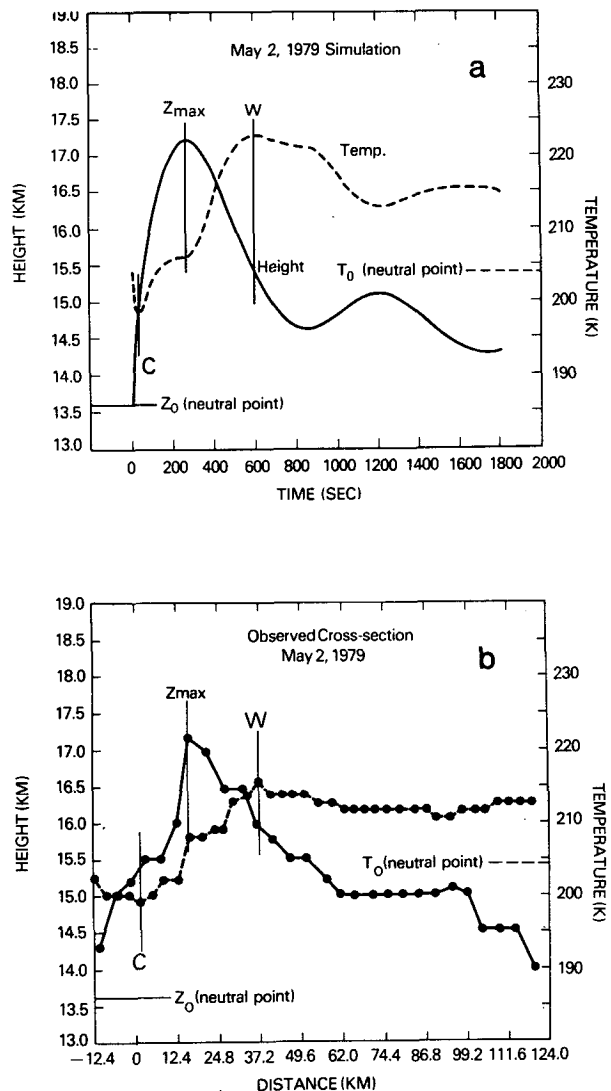


FIG. 18. (a) Parcel model time plot of height (solid) and temperature (dashed) for 2 May 1979 simulation (Fig. 17); (b) cross-section plot of observed stereoscopic height (solid) and IR T_B (dashed) for storm top in Fig. 4.

gradient for this case may be coincidental, but if shown in additional cases would provide a method to determine the location of the high point, which is better related to the location of the radar echo (Hasler, 1981; Heymsfield et al., 1983a). The warm point (W) is located near the upwind side of the general warm area (500–900 s in the model and 35–55 km in the observations). The model parcel temperature remains significantly warmer than the neutral point temperature similar to the IR T_B in the observations. These temperatures warmer than the environment are related to the overshooting of the parcel on its downward path and the following slow process of the parcel coming into equilibrium with the ambient temperature.

Figure 19a gives a schematic view of a cross section through the storm being discussed based on the observations and model results. Figure 19b presents a plot of the parcel temperature–height trajectory based on the parcel model run in Fig. 17 except it is modified subjectively after the warm point assuming that the drag will decrease and the effect of the perturbation pressure terms will also decrease. The dashed trajectories in each part of Fig. 19 are indicative of updraft core parcels ascending to the cloud summit, then descending into the main body of the downwind anvil. The solid-line trajectories in Fig. 19 are very similar to the dashed, except that the descent ends at a higher height and the parcel then slowly oscillates in height while approaching ambient temperature. In the left-hand schematic (Fig. 19a), the solid-line trajectory is pictured as the upper edge of the elevated downwind anvil. A reasonable alternative interpretation would have that same trajectory associated with “above-anvil cirrus,” similar to the interpretation of Fujita (1982) for this case and others. Fujita (1982) postulates that the above-anvil cirrus is the cause of the warm area, whereas our interpretation is that the close-in warm area is due primarily to the subsidence overshooting and that the elevated anvil cloud or the above-anvil cirrus is a by-product of the dynamics and mixing and is a contributor to the observed T_B pattern farther downwind. The primary mechanism for the distinct, close-in warm point is the subsidence and mixing.

The model simulation appropriate for the Wichita Falls, Texas, storm on 10 April 1979 (Fig. 3, storm at the southwest end of the line of thunderstorms) is given in Fig. 20 as the solid line. An isothermal lapse rate and the height and temperature of the parcel neutral point have been chosen based on the analysis of Negri (1982). The parameter α has been adjusted to 0.1 to achieve a maximum height of 15.7 km, approximately the height of the stereo estimate (Fig. 3). The large value of mixing ($\mu_T = 1.0 \text{ km}^{-1}$) and a drag of 0.02 m

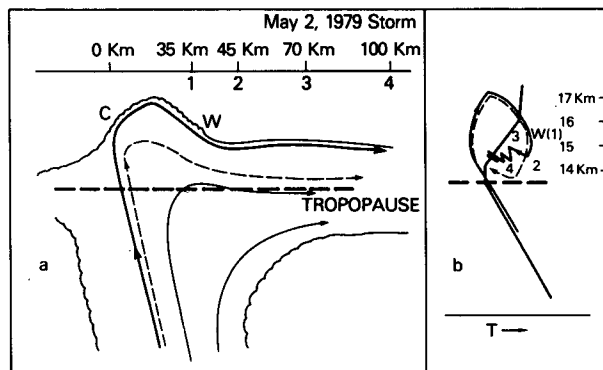


FIG. 19. Schematic of storm top and parcel trajectory for 2 May 1979 storm (Fig. 4).

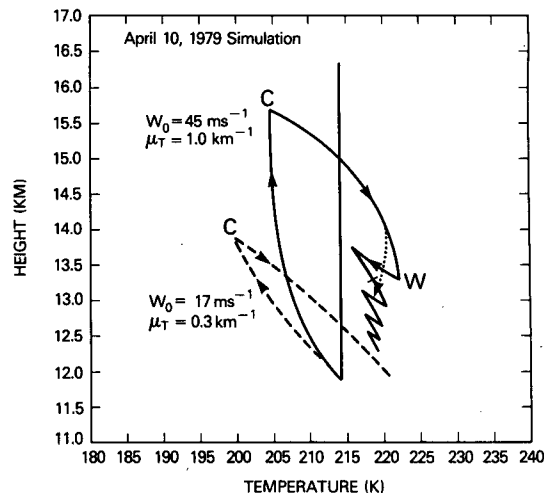


FIG. 20. Parcel model results simulating 10 April 1979 Wichita Falls storm (solid line) and interior storm, both of Fig. 3. $\alpha = 0.10$; $\mu_T = 1.0 \text{ km}^{-1}$.

s^{-2} have been used. This produces a temperature–height parcel path closely resembling earlier isothermal runs [e.g., run (3) in Fig. 8b]. The model time plot is given in Fig. 21a with the corresponding cross section of the T_B and height pattern through the cold and warm points is shown in Fig. 21b. The time to distance conversion in Fig. 21 was generated using the point of maximum height (z_{\max}) in both the model run and observations and the position of the warm point in the observations and the model time of the height of the observed warm point. The resulting speed is 64 m s^{-1} .

The results of the model/observation comparisons in Fig. 21 are not as close as for the 2 May case, primarily because the model warm point is located at a low point near the far end of the general warm area between 500 and 900 s, whereas the observations show the distinct warm point at the near end (closer to z_{\max}) of the general warm area. The simple parcel model cannot produce a warm point along a still descending parcel under isothermal conditions. The Wichita Falls storm was also finishing a period of rapid growth so that the steady state assumptions necessary for the time-space conversions may not be as applicable as in the 2 May case.

The failure of the model to produce a distinct warm point on a downward-sloping path, as is the interpretation of the observations, may also be a basic failure of examining the result of only one parcel trajectory. Since the cirrus anvil downwind of the tower consists of many turbulently mixing parcels, the mean parcel might take the envelope or average path as shown by the dotted segment in Fig. 20. This envelope or average parcel path retains the warm points on the slope. A clearer solution to this point must come from the three-dimensional cloud models.

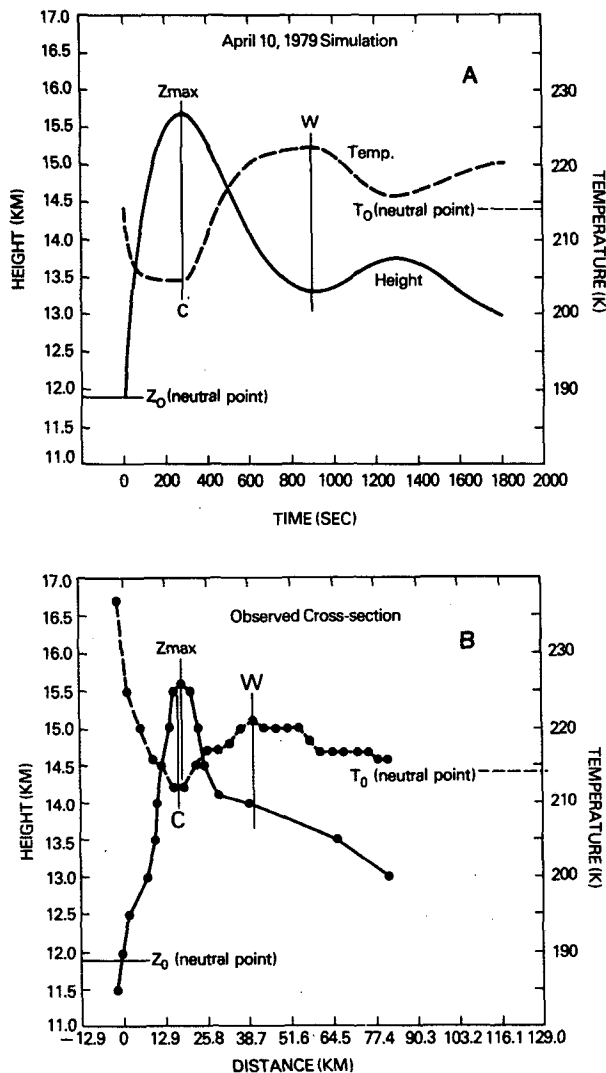


FIG. 21. (a) Parcel model time plot of height (solid) and temperature (dashed) for Wichita Falls simulation (Fig. 3). (b) Cross-section plot of observed stereoscopic height (solid) and IR T_B (dashed) for Wichita Falls storm in Fig. 3.

A second parcel trajectory (the dashed line) is shown in Fig. 20. It is meant to approximately simulate the maximum height (13.8 km) and minimum T_B (205 K, an overestimate of ~ 5 K due to the coarse GOES field of view) of the cloud top with the lack of an associated warm point in Fig. 3. It should also be noted that this "interior" storm has a lower Z_{\max} than the Wichita Falls storm, but a lower T_{\min} . These characteristics are simulated in Fig. 20 by using the small value of mixing ($\mu_T = 0.3 \text{ km}^{-1}$) and a lower w_0 (17 m s^{-1}). The smaller mixing is rationalized by the protected position of the interior storm downwind of the Wichita Falls storm and the lack of a cold-warm couplet itself. With this smaller mixing, which is the only way of obtaining a lower temperature at a lower height than the solid line

in Fig. 20, the model produces reasonable Z_{\max} and T_{\min} values and no warm point. These results emphasize that the T_{\min} values obtained from satellite observations should not be used blindly when assessing thunderstorm intensity.

6. Limitations

The parcel model used in this study is simple and obviously does not have the sophistication to fully reproduce the three-dimensional structure and dynamics of an evolving thunderstorm top. However, it has been shown to crudely reproduce the parcel dynamics of updraft core parcels, but these results must be confirmed by more work of the kind of Schlesinger (1984).

Interpreting the parcel results in terms of the instantaneous image or contour fields of the satellite data is not always obvious. First of all, one has to assume steady state so that the Lagrangian model results can be thought of in the space domain. Second, for those storms with a cold-high offset, the cold point location has been interpreted as on the cloud surface, whereas it could be buried from satellite "view" in the interior of the tower, below the high point. We have assumed that the cold point location on the satellite image is the updraft location at cloud top.

7. Summary

Three classes of thunderstorm overshooting tops have been described from satellite and other observations. Important characteristics of these storm types have been deduced from a simple one-dimensional parcel model.

Typical thunderstorm tops have a monotonic temperature-height pattern with the highest point being the coldest and a collection of storm tops with different maximum heights (above the tropopause) having a maximum height-minimum T_B relation closer to adiabatic than ambient (Class 1). This temperature-height relation is reproduced by the model for low values of mixing, presumed to relate to small values of vertical shear at tropopause level (see schematics in the first panel of Fig. 15).

Two classes of storms with an observed cold-warm IR T_B couplet (25–40 km dimension) have been identified and simulated with the simple model. In the Class 2 storm, the cold point is collocated (or nearly collocated) with the highest point and the warm point is to the rear (downwind) of the highest point. A side-view schematic of this is shown in the second panel of Fig. 15 with parcel trajectories. The left side of the panel shows a schematic of a parcel trajectory in temperature-height space based on the model results. The lack of an inversion precludes the occurrence of a cold-high offset. The occurrence of the warm point is due to the overshooting of the downward-moving parcel in a model storm having a combination of intense mixing

and a strong updraft. Although the observations show the warm point in an area of downward-sloping anvil cirrus, the model cannot reproduce this feature in the absence of an inversion. This explanation is applicable to the example shown in Fig. 3.

As the inversion steepens, the cold-high offset grows until the cold and warm points are at about the same altitude (see Fig. 15c). This is a Class 3 storm and is represented by the example in Fig. 4. Minimum temperature-maximum height plots from the model also indicate that, in these situations, the larger mixing will produce temperature-height relations closer to ambient, in agreement with observations.

The slow oscillations and drift toward the ambient temperature at and after the warm points are interpreted to be related to a downwind portion of the anvil elevated significantly above the original neutral point or above the tropopause. This type of model feature may also be associated with the above-anvil cirrus mentioned by other researchers (e.g., Fujita, 1982) as being related to the occurrence of the warm point. In this study, the warm point is concluded to occur due to the subsidence and overshooting on the downward side and the observed cirrus is the effect of this process, not the cause of the distinct warm point.

The storm top classes discussed in this paper are not meant to be rigid. Individual storms can evolve from one class to another (e.g., Class 1 to Class 3 as the storm matures and penetrates to higher elevations). Intense storms of different classes can exist in the same area or in the same storm complex probably because of the importance of storm-environment interaction in modifying the environments of individual storms. For example, upstream blocking of the tropopause-level ambient flow by an earlier storm may create a drastically different shear environment for a second storm. Also, an individual storm, or complex of storms, may modify the lapse rate in the lower stratosphere (creating stronger inversions) so that later storms may produce more dramatic cold-warm couplets.

A better understanding of the dynamics and physics of the thunderstorm top processes will depend on observational studies involving satellite, aircraft and radar data, and cloud modeling calculations such as those by Schlesinger (1984).

REFERENCES

- Adler, R. F., and D. D. Fenn, 1979: Thunderstorm intensity as determined from satellite data. *J. Appl. Meteor.*, **18**, 502-517.
- , and R. A. Mack, 1984: Thunderstorm height-rainfall rate relations for use with satellite rainfall estimation techniques. *J. Climate Appl. Meteor.*, **23**, 280-296.
- , D. D. Fenn and D. Moore, 1981: Spiral feature observed at top of rotating thunderstorm. *Mon. Wea. Rev.*, **109**, 1124-1129.
- , M. J. Markus, A. J. Negri and G. P. Byrd, 1982: Estimating the temperature and height of overshooting thunderstorm tops from geostationary satellite infrared data. *Conf. on Cloud Physics*, Chicago, Amer. Meteor. Soc., 500-503.
- , D. D. Fenn, G. Szejwach and W. E. Shenk, 1983: Thunderstorm top structure observed by aircraft overflights with an infrared radiometer. *J. Climate Appl. Meteor.*, **22**, 579-593.
- , and —, 1985: Detection of severe Midwest thunderstorms using geosynchronous satellite data. *Mon. Wea. Rev.*, **113**, 769-781.
- Danielsen, E. F., 1982: A dehydration mechanism for the stratosphere. *Geophys. Res. Lett.*, **9**, 605-608.
- Fujita, T. T., 1982: Principle of stereoscopic height computations and their application to stratospheric cirrus over severe thunderstorms. *J. Meteor. Soc. Japan*, **60**, 355-368.
- Hasler, A. F., 1981: Stereographic observations from geosynchronous satellites: An important new tool for the atmospheric sciences. *Bull. Amer. Meteor. Soc.*, **62**, 194-212.
- Heymsfield, G. M., R. H. Blackmer, Jr. and S. Schotz, 1983a: Upper-level structure of Oklahoma tornadic storms on 2 May 1979. I: Radar and satellite observations. *J. Atmos. Sci.*, **22**, 1740-1755.
- , G. Szejwach, S. Schotz and R. H. Blackmer, Jr., 1983b: Upper-level structure of Oklahoma tornadic storms on 2 May 1979. II: Proposed explanation of V pattern and internal warm region in infrared observations. *J. Atmos. Sci.*, **22**, 1756-1767.
- Holton, J. R., 1973: A one-dimensional cumulus model including pressure perturbations. *Mon. Wea. Rev.*, **101**, 201-205.
- Lemon, L. R., and D. W. Burgess, 1980: Magnitude and implications of high speed outflow at severe storm summits. *Preprints 19th Conf. on Radar Meteorology*, Miami, Amer. Meteor. Soc., 364-368.
- McCann, D. W., 1983: The enhanced-V, a satellite observable severe storm signature. *Mon. Wea. Rev.*, **111**, 887-894.
- Mack, R. A., A. F. Hasler and R. F. Adler, 1983: Thunderstorm cloud top observations using satellite stereoscopy. *Mon. Wea. Rev.*, **111**, 1949-1964.
- Negri, A. J., 1982: Cloud-top structure of tornadic storms on 10 April 1979 from rapid scan and stereo satellite observations. *Bull. Amer. Meteor. Soc.*, **63**, 1151-1159.
- , and R. F. Adler, 1981: Relation of satellite-based thunderstorm intensity to radar-estimated rainfall. *J. Appl. Meteor.*, **20**, 288-300.
- Newton, C. W., 1966: Circulations in large sheared cumulonimbus. *Tellus*, **18**, 699-712.
- Roach, W. T., 1967: On the nature of the summit areas of severe storms in Oklahoma. *Quart. J. Roy. Meteor. Soc.*, **93**, 318-336.
- Schlesinger, R. E., 1980: A three-dimensional numerical model of an isolated thunderstorm. Part II: Dynamics of updraft splitting and mesovortex couplet evolution. *J. Atmos. Sci.*, **37**, 396-420.
- , 1984: Mature thunderstorm cloud top structure: Three-dimensional numerical simulation versus satellite observations. *J. Atmos. Sci.*, **41**, 1551-1570.
- Simpson, J., and V. Wiggert, 1969: Model of precipitating cumulus towers. *Mon. Wea. Rev.*, **97**, 471-489.
- Spinhrne, J. D., M. Z. Hansen and J. Simpson, 1983: The structure and phase of cloud tops as observed by polarization lidar. *J. Climate Appl. Meteor.*, **22**, 1319-1331.